PCCP

Accepted Manuscript

ROYAL SOCIETY OF CHEMISTRY

www.rsc.org/pccp

PCCP

PAPER

Acceleration of convective dissolution by chemical reaction in a Hele-Shaw cell

Received 00th January 20xx,
Accepted 00th January 20xx

DOI: 10.1039/x0xx00000x

www.rsc.org/

Ilia Cherezov[a] and Silvana S. S. Cardoso*[a]

New laboratory experiments quantify the destabilising effect of a second-order chemical reaction on the fingering instability of a diffusive boundary layer in a Hele-Shaw cell. We show that, for a given chemical system, the dynamics of such a reactive boundary layer is fully determined by two dimensionless groups, Da/Ra^2, which measures the timescale for convection compared to those for reaction and diffusion, and C_{Bo}', which reflects the excess of the environmental reactant species relative to the diffusing solute. Results of a systematic study varying C_{Bo}' in the range 0 – 0.1 are presented. It is shown that the chemical reaction increases the growth rate of a perturbation and favours small wavelengths compared to the inert system. A higher concentration of C_{Bo}' not only accelerates the onset of convection, but crucially also increases the transport of the solute by up to 150% compared to the inert system. This increase in solute transfer has important practical implications, such as in the storage of carbon dioxide in saline aquifers.

1 Introduction

Understanding the effects of dissolution and reaction on flow in porous media has received increasing interest due to its industrial application in the geological storage of carbon dioxide (CO_2) – a potential way to reduce CO_2 emissions into the atmosphere[1]. During sequestration, industrial CO_2 is injected into saline aquifers saturated with brine. At depths greater than 800 m below the ground, CO_2 is in its supercritical state and less dense than the surrounding formation water. The supercritical CO_2 rises and spreads forming an immiscible layer above the brine, confined by impermeable cap rock. Some of the CO_2 dissolves across the interface to form an aqueous layer of CO_2-rich brine, which grows by diffusion. This diffusive boundary layer is denser than the surrounding brine, so it becomes unstable and breaks up into fingers that transport the CO_2-rich solution away from the interface. The dissolved CO_2 may also react chemically with minerals of the host rock to form ionic species or precipitates[1]. In order to ensure that appropriate sites are selected for safe, long-term storage of CO_2 it is necessary to understand the effects of dissolution and reaction on the flow and transport of CO_2 in an aquifer.

The convective dissolution of CO_2 has been modelled extensively through theoretical studies[2–5], numerical simulations[3,6–11] and experiments using CO_2[12–14] and other analogue systems[15–18]. These studies have characterised the behaviour of CO_2 by quantifying the time for onset of convection, the development of the convective fingers and the dissolution flux of the solute at the interface[19]. However, the effect of geochemical reaction on the instability has been much less researched. Slow reactions with timescales much greater than the convection of CO_2 have been found to have little influence on the fluid motion, whilst fast acting reactions can either stabilise or enhance convection by altering the density profile of the solution[20]. Precipitation reactions between CO_2-rich brine and solid phase minerals consume and withdraw CO_2 from solution, decreasing the density difference driving convection. Theoretical studies[21–24], numerical simulations[25–28] and experimental analogues[29–31] have quantified the stabilising effect of reaction, which was shown to delay the time for onset of convection, stabilise the boundary layer and inhibit finger growth. Reactions can also play a destabilising role by forming a soluble product that is denser than the reactants. Linear stability analysis has shown that for the destabilisation scenario, convection is enhanced and perturbations grow faster than in the non-reactive case[32]. The dissolution of gaseous CO_2 in aqueous amine[33] and solutions of sodium hydroxide[34] has been observed experimentally. Convective fingers were shown to sink monotonically and to develop faster as the concentration of sodium hydroxide was increased. However, besides such qualitative descriptions there is a lack of experimental results characterising the impact of reaction.

In this paper we experimentally quantify the destabilising effect of a second-order reaction $A + B \rightarrow C$, where a dense soluble product is formed. We describe the experimental and theoretical methodologies in sections 2 and 3, respectively, followed by the results and discussion in section 4. A clear comparison of results between this experimental system and previous work for the case with no chemical reaction is given. The main conclusions of the work and its implications are presented in section 5.

[a] Department of Chemical Engineering and Biotechnology, University of Cambridge, Cambridge CB2 3RA, United Kingdom. E-mail: sssc1@cam.ac.uk

Electronic Supplementary Information (ESI) available: Videos 1 – 4 show the evolution of convective fingers in the domain for the cases presented in Fig.2. See DOI: 10.1039/x0xx00000x

2 Experimental

A two-layer Hele-Shaw cell (see Fig. 1) was used to model a two-dimensional homogenous, isotropic porous medium with horizontal and vertical lengths L_x and L_z respectively. The immiscible two-layer system consisted of an organic upper layer of acetic acid (solute A) dissolved in 4-methyl-2-pentanone (commonly known as MIBK) overlying a lower aqueous layer. The diffusion of acetic acid across the interface into the lower layer increases the local density, driving acid-rich convective fingers to descend into the domain, analogous to the convection of CO_2-rich brine in a saline aquifer. The $A + B \rightarrow C$ reaction of interest was studied using aqueous ammonia (reactant B) in the lower layer to form soluble ammonium acetate (product C). The overall reaction can be summarised as

$$CH_3COOH_{(aq)} + NH_{3(aq)} \rightarrow {NH_4}^+{}_{(aq)} + {CH_3COO}^-{}_{(aq)} \quad (1)$$

The reaction obeys second-order kinetics and is almost instantaneous with a kinetic constant k_r of 10^{11} M^{-1} s^{-1} (at 20°C)[35]. The solutal expansion coefficient for C (14.54 kg m^{-3} M^{-1})[36] is greater than that of A (8.17 kg m^{-3} M^{-1})[37] and B (-7.09 kg m^{-3} M^{-1})[38], so that the formation of product increases the density of the fingers compared to the surrounding fluid and has a destabilising effect on the system.

As the solutions are transparent colourless liquids, the fluid flow was visualised using a pH colour indicator. Indicators act as weak acids or bases and can therefore interfere with the observed fluid patterns[39,40]. In order to ensure that the indicator has no substantial impact on the development of the convective dynamics, the type of colour indicator was carefully selected to capture the full extent of the fingers and accurately characterise the flow[41]. The pKa values for acetic acid and ammonia are 4.75 and 9.25 respectively. This means that solutions with pH lower than 4.75 will have acetic acid molecules as the dominant chemical species and conversely if the pH is greater than 9.25, ammonia molecules are dominant. For the intermediate pH region 4.75 – 9.25, ammonium acetate formed as the ionic product of reaction (1) is the dominant species. In order to differentiate between these three distinctive regions a combination of colour indicators was chosen with two pH transition ranges close to 4.75 and 9.25. Solutions were prepared containing a mixture of methyl red ($C_{15}H_{15}N_3O_2$, Mr 269.30) and thymol blue ($C_{27}H_{30}O_5S$, Mr 466.59) indicators, with concentrations of 10^{-6} M. The concentration of indicator used was approximately one hundred times smaller than the lowest initial concentration of ammonia in the lower cell; large enough to yield a sufficient colour contrast between the acidic and basic forms, whilst also being low enough to ensure the effect of indicator on the dynamics of the system to be negligible.

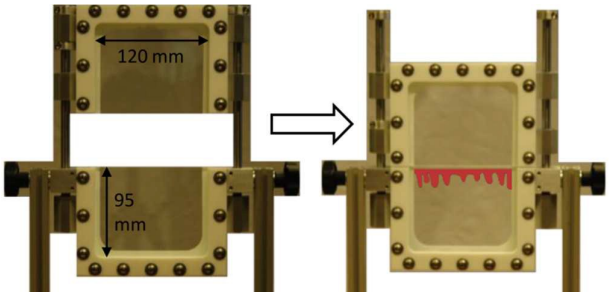

Fig. 1 The Hele-Shaw cell consists of two separate upper and lower cells, based on the design by Kuster *et al.*[40] Each cell uses a pair of borosilicate glass plates (width 120 mm × height 95 mm) secured inside a PTFE frame. The upper cell slides down to rest on top of the lower cell, allowing for the two immiscible fluid layers to come into contact. Acetic acid diffuses across the interface to form convective fingers in the lower cell.

Experiments were carried out at room temperature, with aqueous acid concentration at the top boundary C_{As} = 0.113 M for each case and initial concentration of ammonia C_{Bo} varied in the range 0 – 0.011 M. The value for C_{As} was estimated using equilibrium and mutual solubility data for an acetic acid-MIBK-water system[42] with initial acetic acid concentration in the organic MIBK layer of 0.176 M. The gap thickness between the cell plates was kept constant at h = 1 mm so that the permeability of the cell $k = h^2/12 = 8.3 \times 10^{-8}$ m^2. To start each run, the top cell was slowly lowered causing minimal disturbance of the interface. The domain was illuminated from behind by a LED backlighting panel and the progress of the experiments was recorded at regular one-second intervals using a Nikon D300s camera. IMAGEJ software was used to remove background noise and enhance the contrast of each captured image. Further processing was performed to convert pixels from the RGB to the HSV (Hue, Saturation, Value) colour space[43]. A correlation between the hue-channel pixel intensity and pH was obtained to calculate the pH and thus the concentration of H^+ ions present in each pixel. Using the equilibrium dissociation, mass balance and charge balance equations, it was possible to estimate the total concentration of acid-derived species $C_{AT} = [CH_3COOH] + [CH_3COO^-]$ in each pixel and thus the overall amount of acid transported into the lower cell (Appendix A).

The flows were sufficiently slow for Taylor dispersion in the cell to be negligible and the system is considered to be isothermal as heat effects are much weaker than those due to changes in concentration[44]. Local equilibrium between both phases is assumed so that A dissolves instantaneously with a constant solubility at the top boundary of the lower layer and the dissolution of A is assumed to have no significant effect on the volume. The species B and C are insoluble in the top layer and therefore the focus is on the dynamics only in the lower layer ($z \geq 0$). To avoid bottom boundary effects, the results are presented within a vertical depth of 65 mm from the interface.

3 Theory

3.1 Governing equations

In order to determine the parameters governing the behaviour of the experimental system, we non-dimensionalise the balance equations and boundary conditions below. This will allow a systematic investigation of the relevant parameter space and facilitate comparisons with past and future work. The system is described by the continuity equation (2), Darcy's law (3) and the conservation of the dissolved species with concentration C_i, $i = A, B, C$ (4.a-c).

$$\nabla \cdot \mathbf{v} = 0 \quad (2)$$

$$\mathbf{v} = -\frac{k}{\mu}(\nabla p - \Delta\rho_0 g\mathbf{i}) \quad (3)$$

$$D\nabla^2 C_A - \mathbf{v}\cdot\nabla C_A = \frac{\partial C_A}{\partial t} + k_r C_A C_B \quad (4a)$$

$$D\nabla^2 C_B - \mathbf{v}\cdot\nabla C_B = \frac{\partial C_B}{\partial t} + k_r C_A C_B \quad (4b)$$

$$D\nabla^2 C_C - \mathbf{v}\cdot\nabla C_C = \frac{\partial C_C}{\partial t} - k_r C_A C_B \quad (4c)$$

The fluid viscosity[37] μ = 1.02 × 10^{-3} Pa s and permeability of the medium k are assumed to be constant. The reduced pressure $\nabla p = P - \rho_0 g\mathbf{i}$ is taken to be the difference between the pressure in the liquid P and the hydrostatic pressure. Density changes have been ignored except for the buoyancy term $\Delta\rho_0 g\mathbf{i}$ under the Oberbeck-Boussinesq approximation where $\mathbf{i}$ is vertical unit vector co-directional with the positive z-axis and g = 9.81 m s^{-2}. The density of the aqueous solution ρ is taken to be linearly dependent on concentration C_i so that $\rho = \rho_0 + \beta_A C_A + \beta_B C_B + \beta_C C_C$, where ρ_0 is the reference density and $\beta_i = (\partial\rho/\partial C_i)$ is the solutal expansion coefficient of species i. The density change $\Delta\rho_0 = \rho - \rho_0$ in the buoyancy term can therefore be expressed as $\Delta\rho_0 = \sum \beta_i C_i$.We assume that A, B and C have the same diffusivity[45] D = 1.40 × 10^{-9} m^2 s^{-1}.

3.2 Nondimensionalisation

The equations are nondimensionalised using the scales $L_s = \mu D/(k\beta_A C_{As} g)$, $v_s = D/L_s$, $t_s = {L_s}^2/D$, $p_s = \mu D/k$, C_{As} the concentration of solute A in the aqueous phase at the top boundary of the lower layer (i.e. at the interface), and β_A the solutal expansion coefficient of solute A in the fluid, giving

$$\nabla'\cdot\mathbf{v}' = 0 \quad (5)$$

$$\mathbf{v}' = -\nabla' p' + \sum \beta_i' C_i' \mathbf{i} \quad (6)$$

$$\nabla'^2 C_A' - \mathbf{v}'\cdot\nabla' C_A' = \frac{\partial C_A'}{\partial t'} + \frac{\mathrm{Da}}{\mathrm{Ra}^2} C_A' C_B' \quad (7a)$$

$$\nabla'^2 C_B' - \mathbf{v}'\cdot\nabla' C_B' = \frac{\partial C_B'}{\partial t'} + \frac{\mathrm{Da}}{\mathrm{Ra}^2} C_A' C_B' \quad (7b)$$

$$\nabla'^2 C_C' - \mathbf{v}'\cdot\nabla' C_C' = \frac{\partial C_C'}{\partial t'} - \frac{\mathrm{Da}}{\mathrm{Ra}^2} C_A' C_B' \quad (7c)$$

The initial conditions are $\forall x'$: (C_A', C_B', C_C') = (1, C_{Bo}', 0) for z' = 0 and (C_A', C_B', C_C') = (0, C_{Bo}', 0) for $z' > 0$. At the upper boundary z' = 0, it is set that C_A' = 1 and as $z' \to \infty$, (C_A', C_B', C_C') → (0, C_{Bo}', 0). The boundary conditions are $v_x' = 0$and $\partial C_i'/\partial x'$ at the walls ($x' = 0, L_x/L_s$), and $v_z' = 0$ and $\partial C_i'/\partial z'$ at the bottom ($z' = L_z/L_s$), at all times.

The above analysis suggests that the flow and transport in this system is governed by the following parameters: the dimensionless solutal expansion coefficients of the species β_A', β_B', β_C'; the initial dimensionless concentration of reactant B, C_{Bo}'; and $Da/Ra^2 = k_r C_{As} D/(k\beta_A C_{As} g/\mu)^2$, the ratio of the Damköhler number $\mathrm{Da} = k_r C_{As} {L_z}^2/(D)$ and the square of the solutal Rayleigh number $\mathrm{Ra} = k\beta_A C_{As} g L_z/(\mu D)$. The vertical extent of the reservoir has no effect on the initial development of convection when the reservoir's depth is much greater than the solutal layer thickness, ($L_z \gg L_s$). We shall use these dimensionless groups in the presentation and discussion of our experimental results in section 4.

The solutal expansion coefficients for the acetic acid, ammonia, ammonium acetate system are β_A' = 1.0, β_B' = -0.9, and β_C' = 1.8 respectively, so that the formation of product will have a destabilising effect on the system. In this paper we investigate the effect of varying C_{Bo}', the ratio of the initial concentration of reactant species B (ammonia) in the lower layer and the aqueous concentration of solute A (acetic acid) at the top boundary C_{As}, whilst keeping $\mathrm{Da/Ra^2}$ = 2.9 × 10^7 constant (Ra = 3.4 × 10^4).

4 Experimental results and discussion

Below we present experimental results quantifying for the first time the acceleration of buoyant convection by chemical reaction. We study systematically the distribution of chemical species and its sensitivity to the governing parameters in such system. We also demonstrate for the first time how such reaction affects quantitatively the flow pattern in the reservoir. An image sequence portraying the evolution of convective fingers in the lower layer is shown in Fig. 2 – and in

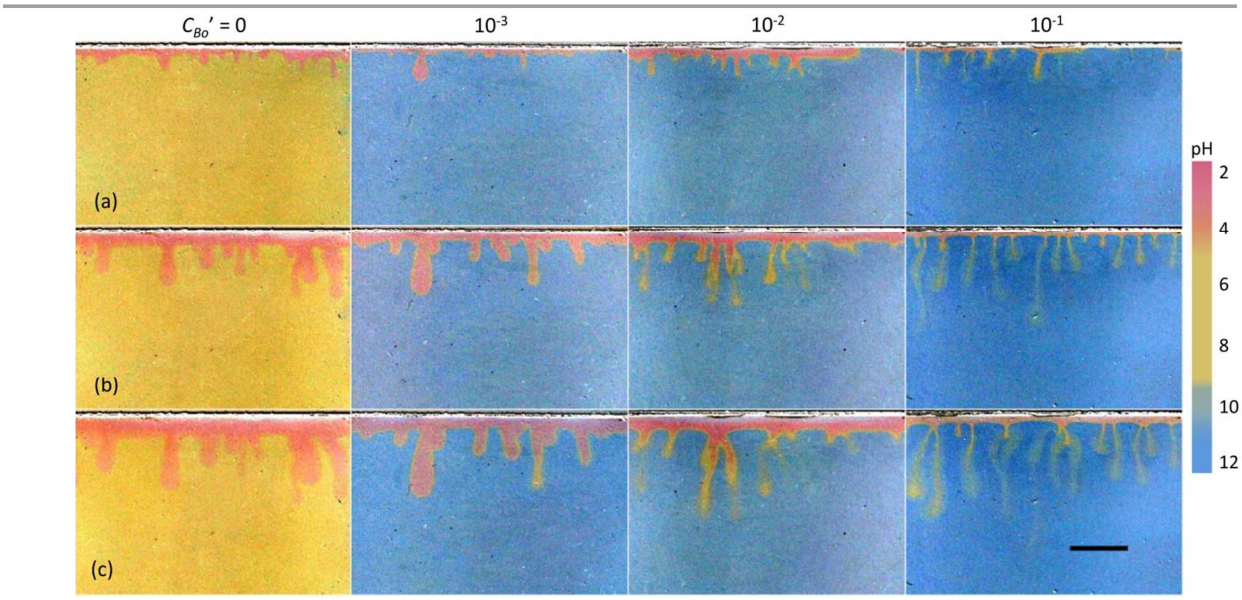

Fig. 2 Sequence of photographs showing the effect of C_{Bo}' on the development of convective instability at dimensionless times (a) t' = 5.0 × 10^4, (b) t' = 2.0 × 10^5, and (c) t' = 3.5 × 10^5. The scaling length L_s = 1.89 x 10^{-6} m is used for each case, and the time and length measurement errors are ±0.5 s and ±0.5 mm respectively. The scale bar represents 20 mm (dimensionless length L' = 10^4). Each picture was edited using IMAGEJ.

supplementary videos available online. The acid A diffuses from the top into the bottom layer forming a boundary layer that grows in thickness with time. Concomitantly, A reacts with the base B present in the lower layer to form the heavy product C. Eventually, this boundary layer becomes unstable, breaking into a number of dense fingers that sink into the bottom layer. There is a sharp visible boundary that separates the fingers, where $C_{AT}' > 0$ and $C_B' = 0$, from the bulk fluid, where $C_{AT}' = 0$ and $C_B' = C_{Bo}'$. Given that the initial concentration of B is much smaller than the concentration of A at the top boundary, depletion of B is rapid compared to the time scale of mixing, and therefore reaction is limited to a narrow region between the solute and the base B. The fingers for the inert case ($C_{Bo}' = 0$) show up red as they are acidic. As C_{Bo}' is increased, neutral yellow-coloured product can be observed to form around the tips and edges of the fingers. With increasing C_{Bo}', the pH of fingers increases and they become more yellow, suggesting that a greater amount of product is formed by reaction. The formation of product is seen to disturb the regular pattern of fingers in the $C_{Bo}' = 0$ and $C_{Bo}' = 10^{-3}$ cases, with the dense product sinking deeper in the domain via thinner and more irregular convective fingers at higher C_{Bo}'.

Transverse-averaged concentration profiles were calculated for the cases shown in Fig. 2 by averaging the concentration field $\langle C_{AT}'(z',t')\rangle = 1/L_x' \int_0^{L_x'} C_{AT}'(x',z',t')\,dx'$ at specific times. The evolution of the average concentration profile in Fig. 3 covers the same dimensionless time range for each case, showing the growth of the solute layer from the top of the domain towards the bottom boundary. As reaction strength increases, the fingers become poorer in A and the heavy product accelerates their downward motion. Convection occurs in a deeper region, but containing only a small concentration of solute A. The diffusive boundary layer for $C_{Bo}' = 10^{-1}$ is narrower than for the other cases in Fig. 3(a) – (c), suggesting that reaction is strong enough to consume the solute and transport the product in rapidly descending fingers before the boundary layer can build up.

The depth of the domain penetrated by convective fingers was calculated from the transverse-averaged concentration profiles. This depth was defined as the value of z' at which the transverse-average concentration $\langle C_{AT}'(z',t')\rangle$ drops below 0.01 and represents the penetration depth of the longest finger. Fig. 4(a) shows the effect of C_{Bo}' on the length of the mixed region as a function of time. After convection is established, the location of the finger front initially advances linearly in time, with the rate increasing as C_{Bo}' increases. As the finger merger and channeling slows down at larger times, the growth rate of the larger fingers decelerates. The inert and weakly reactive cases ($C_{Bo}' = 0$ and 10^{-3}) grow at very similar rates suggesting that the effect of reaction and formation of product is not sufficient to affect the development of the fingers. Convective fingers contain both solute and product species at different concentrations. To differentiate the region where the solute A remains the dominant species, only the parts of the finger with pH less than 4.75 were taken into account in Fig. 4(b). As C_{Bo}' increases the fingers penetrate deeper into the domain when considering the whole finger containing the solute and product. When ignoring the product species for the case of strong reaction ($C_{Bo}' = 10^{-1}$), the solute region slowly grows to approximately $z' = 2 \times 10^3$ in Fig. 4(b) and remains at that depth. This implies that for this case, the fingers sinking deep into the lower aqueous layer predominantly consist of the

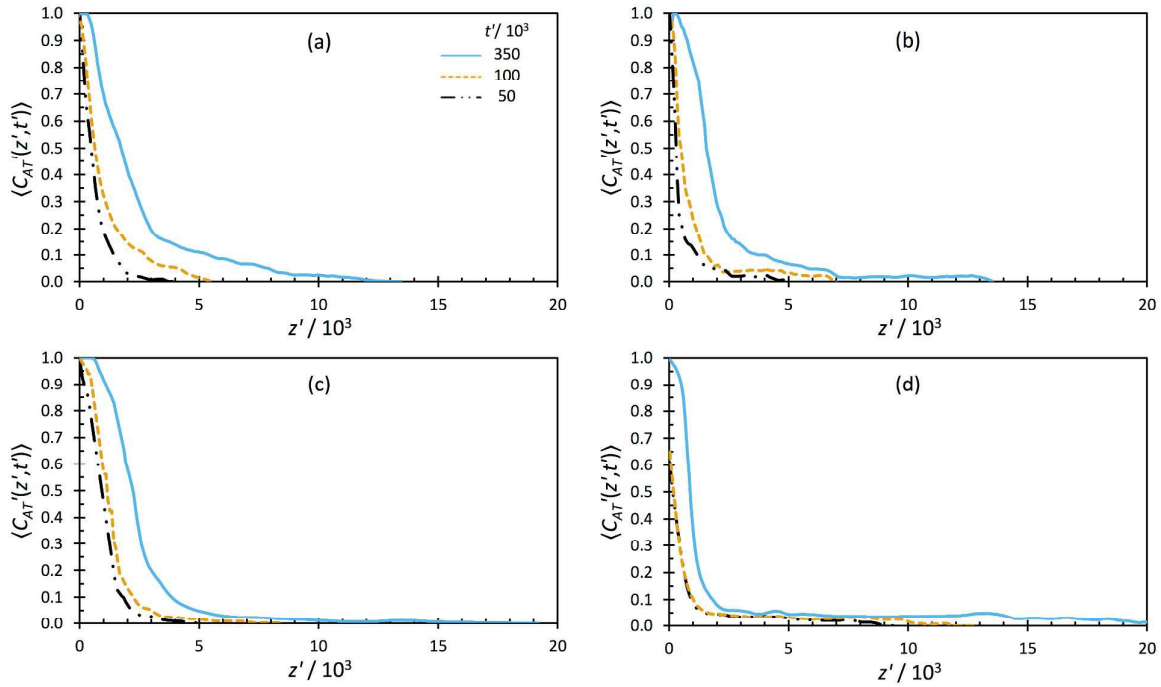

Fig. 3 Transverse-averaged solute concentration profiles $\langle C_{AT}'(z',t')\rangle$ of cases: (a) $C_{Bo}' = 0$, (b) $C_{Bo}' = 10^{-3}$, (c) $C_{Bo}' = 10^{-2}$ and (d) $C_{Bo}' = 10^{-1}$. All four plots cover the same time range $0 \le t' \le 3.5 \times 10^5$, each with the bottom, middle and top curve representing the profile at $t' = 5.0 \times 10^4$, $t' = 1.0 \times 10^5$ and $t' = 3.5 \times 10^5$ respectively.

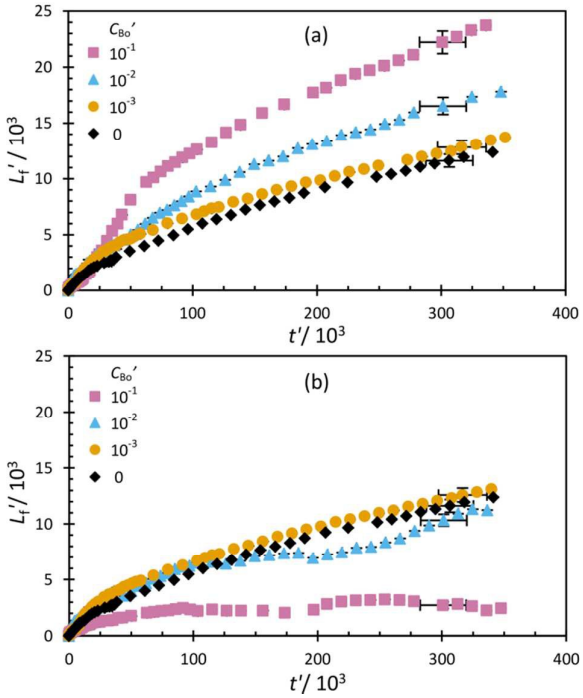

Fig. 4 Evolution of the maximum dimensionless depth of convective fingers L_f' for various C_{Bo}' when considering (a) the whole finger and (b) region of pH ≤ 4.75 where solute *A* is the dominant species.

product of reaction and the formation of product enhances the extent of the mixed layer.

To quantify the interaction between fingers as a function of time, the longitudinal-averaged concentration profiles, $\langle C_{AT}'(x',t')\rangle = 1/L_z' \int_0^{L_z'} C_{AT}'(x',z',t')\,dz'$ were calculated. Each plot in Fig. 5 covers the same dimensionless time range, with the lowest profile taken at the earliest time. As fingers develop in the domain, they are observed to grow individually before merging into fewer, larger fingers. As more solute is transferred and the fingers penetrate deeper into the lower layer, the average concentration can be seen to increase with time. The presence of strong reaction considerably enhances the formation of new fingers over the same period of time, resulting in only a small decrease in the number of fingers in the domain for $C_{Bo}' = 10^{-1}$.

The longitudinal-averaged profiles were decomposed into Fourier modes to quantify the dimensionless averaged wavelength of the fingers $\lambda' = 2\pi/\langle f'(t')\rangle$. The power averaged mean wavenumber[46] was defined as $\langle f'(t')\rangle = \sum f_i' P_i / \sum P_i$ where f_i' are the Fourier modes of the Fast Fourier Transform of the longitudinal-averaged profile and *P(f')* are their amplitudes in Fourier space. As neighbouring fingers merge together during the course of each experiment, the averaged wavelength of instability can be seen to increase as a function of time in Fig. 6. The wavelengths show very similar initial development for all 4 cases studied, until later times where the wavelength for the case of strong reaction ($C_{Bo}' = 10^{-1}$), becomes slightly lower owing to the development of new fingers, as mentioned above.

The time for onset of convection t_{oc}', at which convective fingers were first observed to emerge from the diffusive boundary layer, is plotted in Fig. 7. As expected, the destabilising effect of increasing C_{Bo}' was observed to decrease

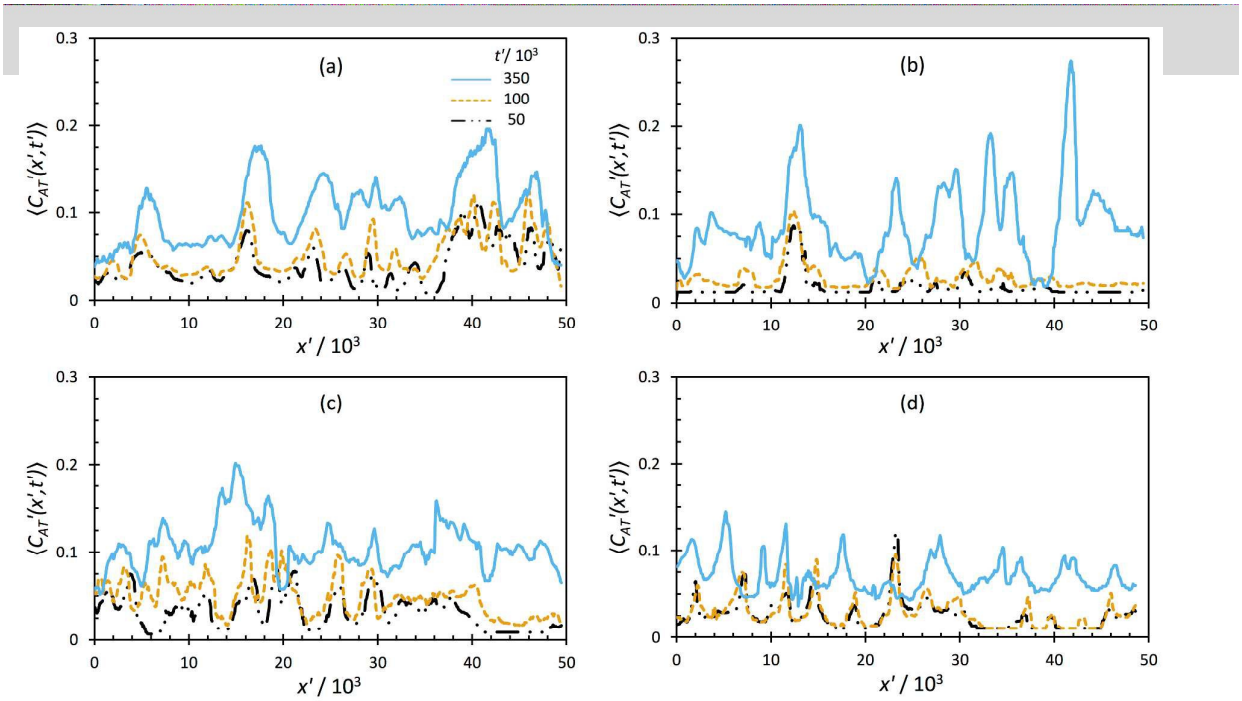

Fig. 5 Longitudinal-averaged solute concentration profiles $\langle C_{AT}'(x',t')\rangle$ of cases: (a) $C_{Bo}' = 0$, (b) $C_{Bo}' = 10^{-3}$, (c) $C_{Bo}' = 10^{-2}$ and (d) $C_{Bo}' = 10^{-1}$. All four plots cover the same time range $0 \le t' \le 3.5 \times 10^5$, each with the bottom, middle and top curve representing the profile at $t' = 5.0 \times 10^4$, $t' = 1.0 \times 10^5$ and $t' = 3.5 \times 10^5$ respectively.

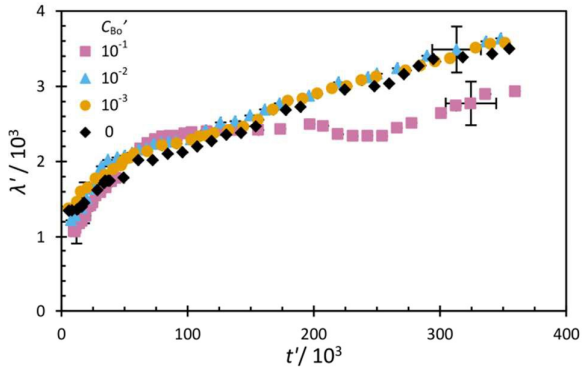

Fig. 6 Dimensionless wavelength of convective fingers λ' as a function of dimensionless time t' for various C_{Bo}'.

the time for onset of convection: fingers develop earlier and descend deeper into the domain as C_{Bo}' is increased. The initial wavelength of fingers at the onset of convection was measured to be $(1.30 \pm 0.28) \times 10^3$. This value appears insensitive to C_{Bo}', but it was difficult to clearly resolve the instabilities at early times. At this initial stage, it is highly likely that fingers have already merged before they become visible.

The dimensionless mass of solute transferred per unit interfacial area $M_A'(t') = 1/L_x' \int_0^{L_z'} \int_0^{L_x'} C_{AT}'(x', z', t')\, dx' dz'$ is shown as a function of dimensionless time in Fig. 8(a). This estimate was made assuming the concentration of B in the environment surrounding the fingers remains approximately constant and equal to C_{Bo}' during the course of an experiment. Measurements of the pH of the bulk fluid deep in the domain away from the fingers and within one finger width from a finger boundary confirm that the pH was constant within the error of the measurement of ± 0.11. It can be seen that all systems rapidly attain a constant mass flux regime, in which M_A' increases linearly as a function of time, with the gradient yielding the dimensionless dissolution flux of solute $J_A' = dM_A'/dt'$ (Fig. 8b). This is the first experimental study to quantify how reaction increases the transport of A into the lower layer, both through accelerated convection and through depletion of A near the interface. A deeper convective zone ensures an efficient transport of A, with the flux in Fig. 8(b) growing by a factor of ~1.5 for each ten-fold increase in C_{Bo}'.

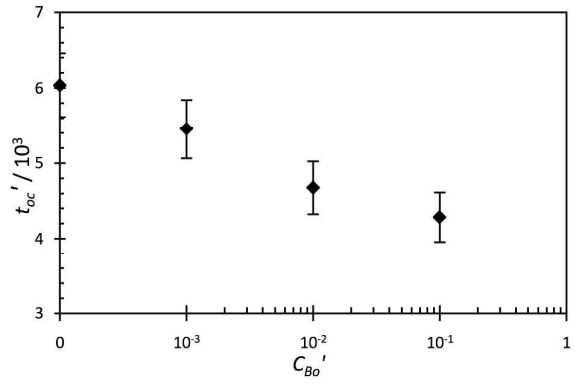

Fig. 7 The effect of C_{Bo}' on the dimensionless time for onset of convection t_{oc}', defined as the time at which convective instabilities were first observed by the naked eye.

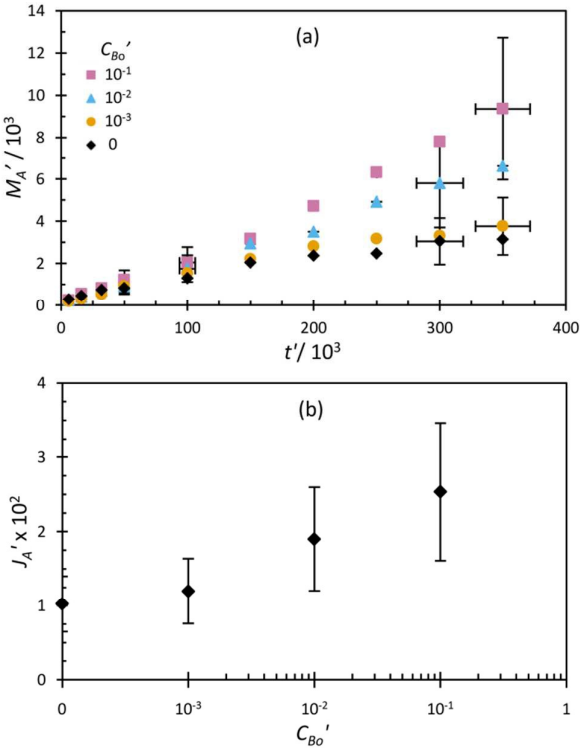

Fig. 8 (a) Dimensionless mass M_A' of solute A transferred to the domain as a function of dimensionless time t' for various C_{Bo}'. (b) Dimensionless mass flux of solute A, $J_A' = J_A L_s/(DC_{As})$ during the constant mass flux regime for various C_{Bo}'.

5 Conclusions

An experimental study of the development of convection in a diffusive boundary layer undergoing a second-order chemical reaction was carried out. Scaling of the governing volume, momentum and chemical balances showed that, for a given chemical system, the boundary behaviour is fully determined by two dimensionless groups: the ratio of the Damköhler number and the square of the solutal Rayleigh number, $\mathrm{Da}/\mathrm{Ra}^2$, and the excess of the environmental reactant species compared to that of the diffusing solute, C_{Bo}'. Importantly, it was shown that the state of mixing in the convective layer depends strongly on the magnitude of C_{Bo}'.

Experimental measurements suggest that for a moderately low chemical concentration ratio, the fingers grow slowly, are rich in the reactant and approximately homogeneous in composition. As the concentration ratio is increased, the heavy reaction product sinks, so that the fingers remain rich in reactant at the top but carry essentially product at the tips; this results in faster-growing, thinner fingers than before. These complex hydrodynamic and chemical interactions lead to faster growth, smaller wavelength and accelerated mass transport in the reactive system compared to that in the inert.

Our findings are important in the geo-storage of carbon dioxide, for which reactions may be engineered to transport products effectively to depth, thereby reducing the risk of an escape of buoyant supercritical carbon dioxide residing in the upper layers of the reservoir.

Appendix

A. Calculation of total acid concentration from pH and pixel intensity to pH calibration

A.1 Equilibrium equations. Acetic acid and ammonia are classed as a weak acid and base respectively, and dissociate in water according to the following equilibrium equations:

$$CH_3COOH \rightleftharpoons CH_3COO^- + H^+ \quad (A1)$$

$$NH_4OH \rightleftharpoons NH_4^+ + OH^- \quad (A2)$$

$$H_2O \rightleftharpoons H^+ + OH^- \quad (A3)$$

The equilibrium constants for each reaction are

$$K_a = \frac{[CH_3COO^-][H^+]}{[CH_3COOH]} = 1.75 \times 10^{-5} \quad (A4)$$

$$K_b = \frac{[NH_4^+][OH^-]}{[NH_4OH]} = 1.75 \times 10^{-5} \quad (A5)$$

$$K_w = [H^+][OH^-] = 1.01 \times 10^{-14} \quad (A6)$$

The equilibrium constant for the overall reaction (1) can be expressed as $K = K_aK_b/K_w = 3.2 \times 10^4$, favouring the production of ammonium acetate.

A.2 Mass and charge balances. The overall charge balance for the dissolved aqueous species is

$$[CH_3COO^-] + [OH^-] = [NH_4^+] + [H^+] \quad (A7)$$

The concentration of all the acetic acid forms present in solution must equal the total concentration of acid added C_{AT}. Some of the acid reacts to form product with concentration C_C and the remaining unreacted acid has concentration C_A. It is assumed that ammonia is evenly distributed in the lower layer and the total concentration of ammonia species C_{BT} is equal to C_{Bo} for each pixel in the domain.

$$C_{AT} = [CH_3COOH] + [CH_3COO^-] = C_A + C_C \quad (A8)$$

$$C_{BT} = [NH_3] + [NH_4^+] = C_{B_0} \quad (A9)$$

Substituting the equilibrium expressions (A4-6) into equations (A8) and (A9):

$$[CH_3COO^-] = \frac{C_{AT}K_a}{[H^+]+K_a} \quad (A10)$$

$$[NH_4^+] = \frac{C_{B_0}K_b[H^+]}{K_w+K_b[H^+]} \quad (A11)$$

The expressions for $[CH_3COO^-]$ and $[NH_4^+]$ can be used to rewrite the charge balance equation (A7) to give:

$$\frac{C_{AT}K_a}{[H^+]+K_a} + \frac{K_w}{[H^+]} = \frac{C_{B_0}K_b[H^+]}{K_w+K_b[H^+]} + [H^+] \quad (A12)$$

Rearranging to make C_{AT} the subject, the total concentration of acid transferred can be expressed as:

$$C_{AT} = \left(1 + \frac{[H^+]}{K_a}\right)\left(\frac{C_{B_0}K_b[H^+]}{K_w+K_b[H^+]} + [H^+] - \frac{K_w}{[H^+]}\right) \quad (A13)$$

Here, $[H^+]$ can be calculated from the pH and the rest of the terms are known constants. We note that a 1% change in K_a, K_b and K_w leads to a 1.8% uncertainty in C_{AT}. Knowing C_{AT}, it is possible to calculate the total mass of acid transferred to the lower layer and thus the mass flux. The concentration of product can be expressed as the concentration of acid that has been neutralised by reaction:

$$C_C = [CH_3COO^-] - [H^+] = \frac{C_{AT}K_a}{[H^+]+K_a} - [H^+] \quad (A14)$$

The concentration of unreacted acid C_A can then be calculated by rearranging (A8) and substituting for C_C:

$$C_A = C_{AT} - C_C = C_{AT} - \frac{C_{AT}K_a}{[H^+]+K_a} + [H^+] \quad (A15)$$

A.3 Pixel intensity to pH calibration. The lower cell, filled with aqueous solutions of known pH and the indicator, was photographed and the resulting images were processed and converted to HSV colour space. The hue (H) channel is able to distinguish between different colour frequencies, whilst the saturation (S) and value (V) channels provide supplementary information on the colour details. The hue-channel pixel intensities were found to vary with pH of the aqueous solution as shown in Fig. 9(a). A one-to-one relationship was observed between the pixel intensity and pH in the low and high pH ranges. In the near neutral range 5 < pH < 9, the solution colour does not change enough to cause a measurable difference in the hue intensity. This limitation is not significant because the concentration of acid required to yield a solution with pH 5-9 is insensitive to the pH, as shown in Fig. 9(b). Indeed, Fig. 9(c) shows that a one-to-one relationship is obtained between the pixel intensity and the total acid concentration C_{AT} for the entire working range of pH in each of the reactive cases investigated.

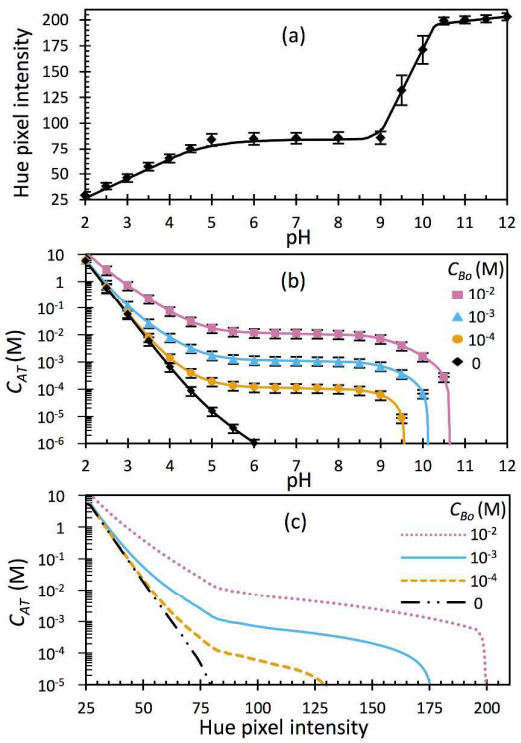

Fig. 9 (a) Hue-channel pixel intensities as a function of the pH of aqueous solutions with indicator. The error bars show the standard deviation in pixel intensity of the domain. (b) Total acid concentration C_{AT} added to solution as a function of pH, calculated using equation (A13). Plots are shown in dimensional form for the different reactive cases and the error bars show the uncertainty in C_{AT} associated with an error in pH measurement of ± 0.11. (c) Relationship between C_{AT} and hue-channel pixel intensities for the different reactive cases.

B. Inert results

B.1 Methods. In order to validate the experimental system and procedure, results for cases with no reaction were compared to previous published work. The lower layer was filled with pure water (C_B', $C_C' = 0$) and combinations of different acid concentrations C_{As} and gap widths were used to investigate cases in the range $5 \times 10^3 < \mathrm{Ra} < 3.5 \times 10^5$.

B.2 Convective mass flux. The dissolution rate of CO_2 has been characterised in dimensionless terms by the Sherwood number $\mathrm{Sh} = J_A L_z/(DC_{As})$. The black diamonds in Fig. 10 present the results for this system showing a sublinear scaling relation between dimensionless convective flux and Rayleigh number $\mathrm{Sh} = (0.040\pm0.018)\mathrm{Ra}^{0.86\pm0.04}$. This agrees with existing numerical[9] and experimental[15–17] results with Ra exponents approximately equal to 0.8, with the slight variations attributed to the error in calculating the convective flux, the differences in fluid systems and experimental setups.

B.3 Convective finger depth. To determine the evolution of the CO_2-rich layer, the vertical extent of the domain penetrated by the tip of the longest solute finger was tracked by measuring the depth at which the transverse-averaged concentration $\langle C_A'(z',t')\rangle$ drops below 0.01. For clarity, the results for 4 different inert cases (Ra = 1.1×10^4, 2.2×10^4, 3.4×10^4, 6.9×10^4) are presented in Fig. 11. The solute layer was observed to initially grow at rate similar to that calculated for a diffusive profile before convection dominates and fingers show linear growth consistent with previous work. The linear growth of convective fingers was later observed to slow down as previously seen by Slim[10], where the pioneer plumes, penetrating deepest into the domain, were found to decelerate during the constant flux regime (for $t' \approx 1.6 \times 10^3$). Despite the differences in the concentrations and gap widths between the inert cases, it is apparent that they show the same result after nondimensional scaling.

B.4 Convective finger wavelength. The four inert cases again show very similar results after scaling in Fig. 12. The evolution of the dimensionless wavelength compares well to the results of existing experiments[12], but is larger than that calculated by numerical simulations. This is most likely due to the fact that some finger mergers may have already occurred before the instabilities become visible in experiments, giving rise to a larger wavelength.

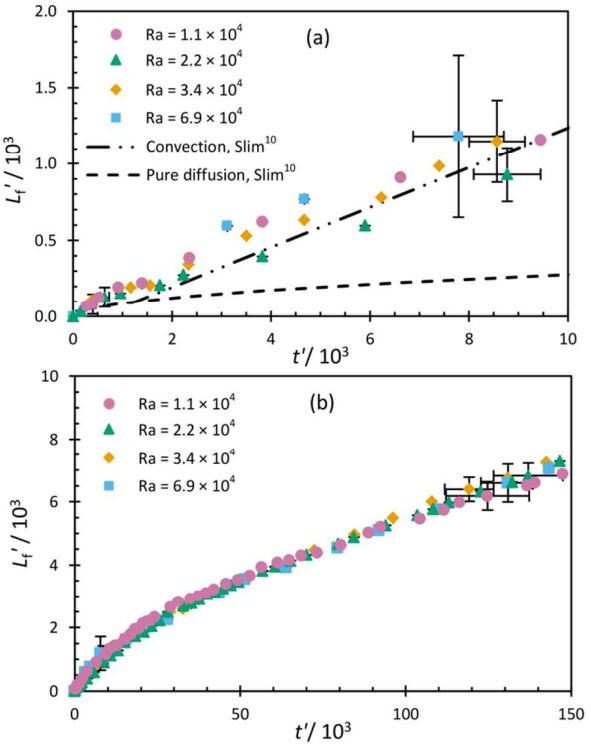

Fig. 11 Evolution of the maximum dimensionless depth of convective fingers L_z' for various inert-system cases at (a) dimensionless time $0 \le t' \le 1.0 \times 10^4$ and (b) $0 \le t' \le 1.5 \times 10^5$. Previous numerical simulations for the maximum finger depth for solutal convection and pure diffusion, (from Fig. 5 of Slim[10]) are shown in (a).

B.5 Time for onset of convection. Numerical studies have reported dimensionless times for onset of convection ranging from $t_{oc}' = 8.50 \times 10^2$ (Ghesmat *et al.*[25]) to $t_{oc}' = 5.62 \times 10^3$ (Hidalgo and Carrera[7]). The observed $t_{oc}' \approx (6.17 \pm 0.49) \times 10^3$ for this system is slightly larger than the previously determined values, but this overestimation is within the uncertainty

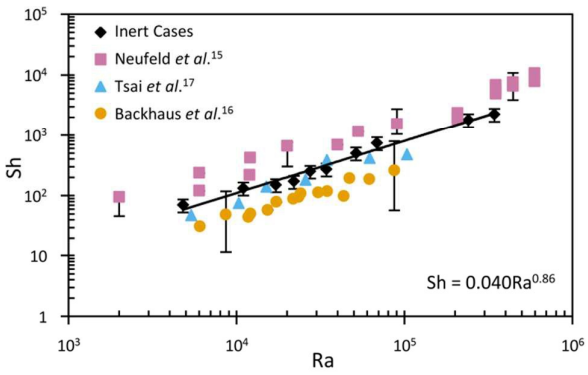

Fig. 10 Dimensionless convective flux expressed as the Sherwood number, $\mathrm{Sh} = J_A L_z/(DC_{As})$, as a function of Rayleigh number, Ra, for different inert systems. The solid line is the best power-law fit of the form $\mathrm{Sh} = (0.040 \pm 0.018)\mathrm{Ra}^{0.86 \pm 0.04}$ for the inert system presented in this paper.

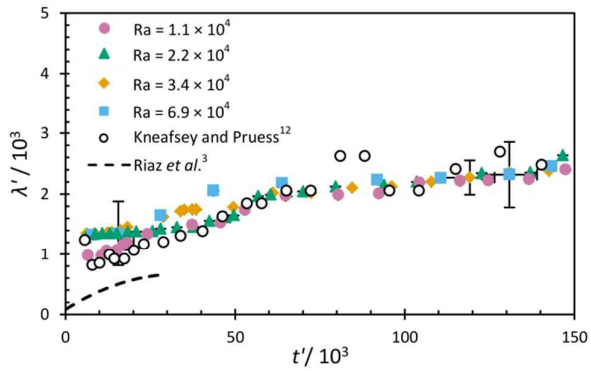

Fig. 12 Dimensionless wavelength of convective fingers λ' as a function of dimensionless time t' for various inert system cases. Previous experimental (from Fig. 4, Kneafsey and Pruess[12]) and numerical results (Fig. 11, Riaz *et al.*[3]) are also shown.

associated with differentiating early convective fingers by the naked eye.

These comparisons above validate the experimental system and methodology proposed in this paper to study the more complex reactive system.

Acknowledgements

I.C. is grateful for financial support from the EPSRC.

References

1 IPCC, *Special Report on Carbon Dioxide Capture and Storage*, Cambridge University Press, United Kingdom and New York, NY, USA, 2012.
2 J. Ennis-King, I. Preston and L. Paterson, *Phys. Fluids*, 2005, **17**, 084107.
3 A. Riaz, M. Hesse, H. A. Tchelepi and F. M. Orr, *J. Fluid Mech.*, 2006, **548**, 87.
4 D. A. S. Rees, A. Selim and J. P. Ennis King, *Emerging Topics in Heat and Mass Transfer in Porous Media*, Springer, Netherlands, 2008, pp. 85-110.
5 M. Chan Kim and C. Kyun Choi, *Phys. Fluids*, 2012, **24**, 044102.
6 H. Hassanzadeh, M. Pooladi-Darvish and D. W. Keith, *AIChE J.*, 2007, **53**, 1121-1131.
7 J. J. Hidalgo and J. Carrera, *J. Fluid Mech.*, 2009, **640**, 441.
8 G. S. H. Pau, J. B. Bell, K. Pruess, A. S. Almgren, M. J. Lijewski and K. Zhang, *Adv. Water Resour.*, 2010, **33**, 443-455.
9 R. Farajzadeh, B. Meulenbroek, D. Daniel, A. Riaz and J. Bruining, *Comput. Geosci.*, 2013, **17**, 515-527.
10 A. C. Slim, *J. Fluid Mech.*, 2014, **741**, 461-491.
11 M. Chan Kim, *Chem. Eng. Sci.*, 2015, **126**, 349-360.
12 T. J. Kneafsey and K. Pruess, *Transp. Porous Media*, 2010, **82**, 123-139.
13 T. F. Faisal, S. Chevalier, Y. Bernabe, R. Juanes and M. Sassi, *Int. J. Heat Mass Transf.*, 2015, **81**, 901-914.
14 R. Nazari Moghaddam, B. Rostami and P. Pourafshary, *Chem. Eng. Commun.*, 2015, **202**, 815-822.
15 J. A. Neufeld, M. A. Hesse, A. Riaz, M. A. Hallworth, H. A. Tchelepi and H. E. Huppert, *Geophys. Res. Lett.*, 2010, **37**, L22404.
16 S. Backhaus, K. Turitsyn and R. E. Ecke, *Phys. Rev. Lett.*, 2011, **106**, 104501.
17 P. A. Tsai, K. Riesing and H. A. Stone, *Phys. Rev. E: Stat., Nonlinear, Soft Matter Phys.*, 2013, **87**, 011003.
18 A. C. Slim, M. M. Bandi, J. C. Miller and L. Mahadevan, *Phys. Fluids*, 2013, **25**, 024101.
19 H. Emami-Meybodi, H. Hassanzadeh, C. P. Green and J. Ennis-King, *Int. J. Greenhouse Gas Control*, 2015, **40**, 238-266.
20 J. Ennis-King and L. Paterson, *Int. J. Greenhouse Gas Control*, **1**, 86-93.
21 D. Pritchard and C. N. Richardson, *J. Fluid Mech.*, 2007, **571**, 59-95.
22 L. T. Ritchie and D. Pritchard, *J. Fluid Mech.*, 2011, **673**, 286-317.
23 M. Chan Kim and C. Kyun Choi, *Phys. Rev. E*, 2014, **90**, 53016.
24 T. J. Ward, K. A. Cliffe, O. E. Jensen and H. Power, *J. Fluid Mech.*, 2014, **747**, 316-349.
25 K. Ghesmat, H. Hassanzadeh and J. Abedi, *J. Fluid Mech.*, 2011, **673**, 480-512.
26 J. T. Andres and S. S. Cardoso, *Phys. Rev. E,* 2011, **83**, 046312.
27 J. T. Andres and S. S. Cardoso, *Chaos*, 2012, **22**,
28 T. J. Ward, O. E. Jensen, H. Power and D. S. Riley, *J. Fluid Mech.*, 2014, **760**, 95-126.
29 K. Eckert, M. Acker and Y. Shi, *Phys. Fluids*, 2004, **16**, 385-399.
30 S. S. Cardoso and J. T. Andres, *Nat. Commun.*, 2014, **5**, 5743.
31 M. A. Budroni, L. A. Riolfo, L. Lemaigre, F. Rossi, M. Rustici and A. De Wit, *J. Phys. Chem. Lett.*, 2014, **5**, 875-881.
32 V. Loodts, L. Rongy and A. De Wit, *Phys. Chem. Chem. Phys.*, 2015, **17**, 29814-29823.
33 C. Wylock, A. Rednikov, B. Haut and P. Colinet, *J. Phys. Chem. B*, 2014, **118**, 11323-11329.
34 V. Loodts, C. Thomas, L. Rongy and A. De Wit, *Phys. Rev. Lett.*, 2014, **113**, 114501.
35 S. Someya, S. Yoshida, T. Tabata and K. Okamoto, *Int. J. Heat Mass Transfer*, 2009, **52**, 4236-4243.
36 O. Sohnel, P. Novotny and Z. Solc, *J. Chem. Eng. Data*, 1984, **29**, 379-382.
37 A. Wolf, *Aqueous Solutions of Body Fluids – Their Concentrative Properties and Conversion Tables*, Harper & Row Publishers, New York and London, 1966.
38 P. Novotny and O. Sohnel, *J. Chem. Eng. Data*, 1988, **33**, 49-55.
39 C. Almarcha, P. M. J. Trevelyan, L. A. Riolfo, A. Zalts, C. El Hasi, A. D'Onofrio and A. De Wit, *J. Phys. Chem. Lett.*, 2010, **1**, 752-757.
40 S. Kuster, L. A. Riolfo, A. Zalts, C. El Hasi, C. Almarcha, P. M. Trevelyan, A. De Wit and A. D'Onofrio, *Phys. Chem. Chem. Phys.*, 2011, **13**, 17295-17303.
41 C. Thomas, L. Lemaigre, A. Zalts, A. D'Onofrio and A. De Wit, *Int. J. Greenhouse Gas Control*, 2015, **42**, 525-533.
42 T.K. Sherwood, J. E. Evans and J. V. A. Longcor, *Ind. Eng. Chem.*, 1939, **31**, 1144-1150.
43 A. R. Smith, *SIGGRAPH Comput. Graph.*, 1978, **12**, 12-19.
44 C. Almarcha, P. M. Trevelyan, P. Grosfils and A. De Wit, *Phys. Rev. E*, 2013, **88**, 033009.
45 *CRC Handbook of Chemistry and Physics*, ed. R. C. Weast and M. J. Astle, 59th edn, CRC Press, Boca Raton, FL, 1979.
46 W. B. Zimmerman and G. M. Homsy, *Phys. Fluids A*, 1991, **3**, 1859.